FEDSM-ICNMM2010-' ‰ -

PIV STUDY OF THE NEAR-FIELD REGION OF A TURBULENT ROUND JET

Ivana M. Milanovic
University of Hartford
West Hartford, CT, USA

Khaled J. Hammad
Dantec Dynamics, Inc.
Ramsey, NJ, USA

ABSTRACT

Turbulent jets have been extensively studied in the past due to their fundamental importance and wide spread usage in numerous industrial processes to enhance momentum, heat and mass transfer. Most previous work focused on the far-field or self-similar region of the flow. However, the initial development region, where the flow is dominated by streamwise and large-scale, Kelvin-Helmholtz-type, structures, received far less attention. In the current study, Particle Image Velocimetry (PIV) was used to obtain reliable statistics in the near-field region of a turbulent submerged jet. The jet issued from an 84 diameter, D, long pipe which ensured fully-developed turbulent flow conditions at the outlet. The two-dimensional flow field in the plane containing the jet axis was measured in the initial $8D$ region, for three Reynolds numbers: 14,602, 19,135, and 24,685. The selected Reynolds numbers overlap with the previously identified critical Reynolds number range, 10,000-20,000, where flow characteristics of a jet undergo a dramatic transition to a much more chaotic and well-mixed state or fully developed turbulence.

NOMENCLATURE

D	Pipe internal diameter (m)
H	Pipe-to-plate separation distance (m)
J	Jet momentum
L	Pipe length (m)
M	Mass flow rate
Re	Reynolds number ($U_b D/\nu$)
U	Mean velocity magnitude (m/s)
U_c	Mean centerline velocity at the pipe exit (m/s)
U_b	Pipe bulk velocity (m/s)
r, z	Cylindrical coordinates (m)
u_r, u_z	Instantaneous velocity in r and z directions (m/s)
u_r', u_z'	Velocity fluctuations in r and z directions (m/s)
$\overline{u_r'^2}, \overline{u_z'^2}$	Normal Reynolds stresses (m^2/s^2)
$\overline{u_r'u_z'}$	Shear Reynolds stress (m^2/s^2)
$u_{r,rms}$	Normalized RMS velocity $\sqrt{\overline{u_r'^2}}\big/U_c$ in r direction
$u_{z,rms}$	Normalized RMS velocity $\sqrt{\overline{u_z'^2}}\big/U_c$ in z direction

Greek Symbols

ρ	Density
ν	Kinematic viscosity of jet fluid (m^2/s)
ω	Vorticity normalized by $2\pi U_b/D$

Subscripts

c	Centerline
e	Initial
j	Jet
p	Pipe
r	Radial
z	Vertical

INTRODUCTION

Turbulent jet flows have a variety of technically important applications such as cooling/heating, drying, mixing and

chemical vapor deposition (CVD). Jet flows are also commonly studied shear flows for the purpose of turbulence modeling. Their practical and fundamental significance resulted in a large volume of theoretical, experimental and numerical research targeting specific flow regions. Based on the characteristics of the velocity field the axisymmetric round jet has three regions: the near-, the intermediate- and the far-field. The near-field with flow characteristics similar to those at the jet exit is usually found within $0 \leq x/D \leq 6$. In the far-field region the flow has reached a dynamic equilibrium and properly scaled cross-stream mean and RMS profiles collapse. Jets generally become fully-developed or self-similar beyond $x/D \geq 25$. The intermediate or transition region lies between the near- and far-fields of the jet. The near- and intermediate-fields comprise the development portion of the jet and significantly influence the downstream evolution of the jet in its numerous applications.

The mixing of scalar is observed to change dramatically near a critical Reynolds number. Mixing transition for jet was characterized qualitatively by flow visualizations in Dimotakis *et al.* [1] indicating differences in the scalar field below and above Reynolds number of 10,000-20,000. In his review article Dimotakis [2] relied upon scalar measurements and qualitative observations to identify the mixing transition in jets. The notion that a mixing transition should be universal implies existence of a transitional Reynolds number for jet flows.

A comprehensive review of the experimental and numerical studies performed to date on a round jet may be found in Ball and Pollard [3]. This literature survey indicated a dearth of data in the near- and intermediate-fields of a round jet for a Reynolds number range corresponding to the mixing transition. A summary of the studies in the developing region of axisymmetric turbulent jet relevant to the mixing transition is now presented. The two nozzle types are commonly used to generate jet flow: smoothly contracting (contoured) nozzles and long pipes producing nearly uniform 'top-hat' and non-uniform fully-developed velocity profiles, respectively.

Fellouah *et al.* [4] investigated the effect of Reynolds number on the mixing transition of a free round jet with top-hat velocity profile. Flying and stationary hot-wire measurements were made for Reynolds numbers of 6,000, 10,000, and 30,000 at a range of axial positions, x/D, from 0 to 25. The transition Reynolds number was found to be above 20,000.

Shinneeb *et al.* [5] used particle image velocimetry (PIV) and proper orthogonal decomposition (POD) to investigate large-scale structures in the near-field ($0 \leq x/D \leq 2.2$) of jet with top-hat velocity profile and Reynolds number 21,900.

Jung *et al.* [6] carried out hot-wire measurements in the near-field ($2 \leq x/D \leq 6$) of jet issuing from nozzle at Reynolds numbers of 78,400, 117,600, and 156,800. The POD modes showed the evolution of the three dimensional streamwise velocity field from 'volcano-type' eruptions at x/D = 2-3 to 'propeller-like' blade patterns where the number of blades diminish with the downstream distance.

Ganapathisubramani *et al.* [7] performed PIV study of round jet in the near-field region at Reynolds number of 19,000

for the purpose of comparing four vortex identification schemes. Vortex cores were found to form as early as $x/D \approx$ 0.5. Their downstream evolution led to the vortex pairing up and creation of larger-scale structures.

Ferdman *et al.* [8] reported hot-wire measurements ($0 \leq x/D \leq 80$) of jet issuing from straight pipe and a bend at Reynolds number of 24,000. They found that the initial growth of turbulence intensities is higher for uniform initial-velocity profiles.

Papadopoulos and Pitts [9-10] used Rayleigh light scattering (RLS) to examine centerline mixing behavior in the near-field of constant and variable-density jets issuing from pipe. The initial turbulence intensity per unit area was identified as controlling parameter and new length scales were introduced.

Weisgraber and Liepman [11] used PIV to measure the development of turbulence and vorticity in the transitional region $15 \leq x/D \leq 30$ of jet issuing from a nozzle at Reynolds numbers of 5,500 and 16,000. Reynolds number was shown to influence the flow structure and the rate of jet development.

Boguslawski and Popiel [12] used cross-wire probes to examine the structure of the free pipe jet in the initial region ($0 \leq x/D \leq 12$) at Reynolds numbers of 51,000 and 125,000.

Most comparative studies investigating the effect of inlet profiles on jet development are done for singular Reynolds number: Xu and Antonia [13] carried out ×-wire measurements in $1 \leq x/D \leq 75$ range at Reynolds number of 86,000; Antonia and Zhao (2001) examined downstream effects at x/D = 0, 2, 30 and 50 and Reynolds number of 37,000; Mi *et al.* (2001) [14-15] performed both flow visualizations using the Mie scattering and ×-wire measurements to reveal the evolution of the scalar field in the range $0 \leq x/D \leq 70$ and for Reynolds number of 16,000.

Richards and Pitts [16] used Rayleigh light scattering (RLS) to examine the effects of initial velocity profile and global density ratio in $10 \leq x/D \leq 60$ range and at Reynolds number of 4,000 and 25,000. It was shown that regardless of the initial velocity profile, axisymmetric turbulent free jets decay at the same rate, spread at the same half-angle, and both the mean and RMS values collapse in a form consistent with full self-preservation.

Computational studies in the mixing transition regime have not been abundant either. The general experience and lessons gained from these investigations are summarized below, followed by a brief description of the works pertaining to the physical characterization of the flow-field. Direct numerical simulations (DNS) resolve all the scales of the flow; however, they are resource consuming and limited to low Reynolds number turbulent flows in small regions. Large eddy simulations (LES) solve for unique large eddies while the universal effect of the smaller eddies is modeled.

Bogey and Bailly [17] employed LES to study the near-field ($0 \leq x/D \leq 12$) of round jet in a range of Reynolds numbers. While the Reynolds number was shown to have a

significant influence on the flow characteristics, its values were either below (10,000) or far above (400,000) the mixing transition range proposed by Dimotakis [1-2].

McIlwain and Pollard [18] carried out LES study in the near-field of round free jet both with and without swirl. The jet nozzle produced top-hat velocity profile with a Reynolds number of 68,000.

Olsson and Fuchs [19] used LES to examine the near-field region ($3 \leq x/D \leq 9$) of a confined round jet at Reynolds numbers of 10,000, 50,000 and 500,000. Again, Reynolds number dependence was demonstrated for values outside of the range where mixing transition takes place.

It is apparent that the database of flow characteristics in the near- and intermediate-fields of a round jet for a Reynolds number spanning the mixing transition regime is not complete. The objective of the current work is to study the development region of a submerged water jet. Two components of the mean and RMS velocity were obtained using PIV. The two-dimensional flow field in the plane containing the jet axis was measured at locations between 1 and 8D downstream, for three Reynolds numbers: 14,602, 19,135 and 24,685. A fully developed jet inflow condition allow for assessment of turbulence models and numerical schemes. The experimental setup and test conditions are described next.

EXPERIMENTAL SETUP

The closed-loop system is comprised of a water tank, pump, tube and tube mounting and positioning structure. The rectangular glass tank used was 406 mm long, 203 mm wide and 254 mm high. The tank walls were approximately 6 mm thick. The jet was produced using a vertical type 316 stainless steel precision pipe placed on the cylinder centerline with an inner diameter D = 10.92 mm, a length L = 914.4 mm and a wall thickness 0.889 mm. The length-to-diameter ratio of the pipe, L/D = 84, assured a fully developed turbulent flow conditions at the outlet. The jet was placed 102 mm, about 9.3D, away from the side walls of the tank and 208 mm, about 19D, from the tank bottom. The filled height of the tank was 240 mm, 22D.

As shown in Fig. 1, the origin of the cylindrical r,z coordinate system coincides with the center of the pipe right at the exit plane and the z axis pointing vertically downward.

Measurements were performed for three different Reynolds numbers. Three volumetric flow rates of 16.25×10^{-5} m³/s (2.58 GPM), 12.6×10^{-5} m³/s (2 GPM), 9.83×10^{-5} m³/s (1.56 GPM), were used, resulting in fixed pipe bulk velocities, U_b, of 1.74, 1.35, and 1.05 m/s. The corresponding kinematic viscosities of the working fluid, tap water, were 7.68×10^{-7} (32°C), 7.68×10^{-7} (32°C), and 7.85×10^{-7} m²/s (32°C). The Reynolds numbers, $\mathrm{Re} = U_b D / \nu$, were 24,685, 19135, and 14,602.
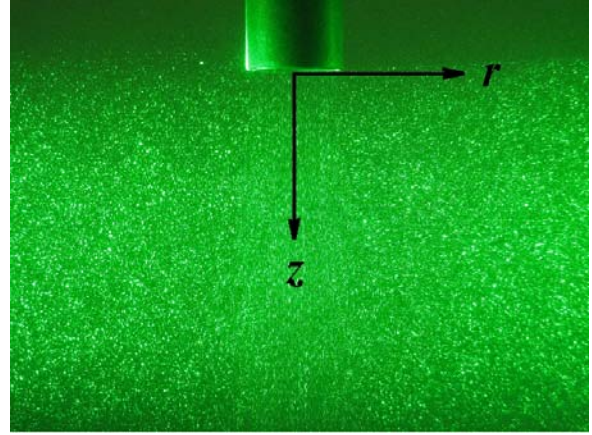

Fig.1 Coordinate System

PIV SYSTEM AND DATA PROCESSING

A DANTEC DYNAMICS two-dimensional PIV system was used to measure the flow field along each r-z plane of interest. The system consisted of synchronization hardware for controlling the laser and camera, and software running on a Windows-based platform for data acquisition, management and post-analysis. The light source was a New-Wave Research Pegasus® dual-head, diode-pumped Nd:YLF laser system. Each laser head was capable of operating between 1 and 10,000 pulses per second. When fired at 1kHz, the resulting per-cavity energy at 527nm is 10mJ. A Phantom® v210, 1 megapixel high-speed camera capable of taking more than 2,000 frames-per-second (fps) at full 1280 x 800 pixel resolution was used. The CMOS camera has an active pixel size of 20 microns and 8- and 12-bit pixel depth.

The Nd:YLF laser was fired at a frequency of 100 Hz, yielding 200 pulses of green (527-nm wavelength) 1.5 mm beams, each having a typical pulse duration of about 180 ns. Light sheet forming optics mounted at the exit portal of the laser system generated a thin, focusable light sheet by means of a series of spherical and cylindrical lenses. A vertical divergent light sheet was used to illuminate the full extent of the measurement region within the cylindrical tank. The vertical light sheet was aligned to pass through the center of the pipe. The thickness of the light sheet at the imaging plane was 1 mm. The spatial location of the illumination system was fixed during all the tests. The CMOS camera was placed perpendicular to the laser sheet. The lens used was a 60-mm f2.8 Nikkor. The imaged field of view was 153 x 96 mm, at a magnification coefficient of 0.167.

The seeding particles used were 50 μm diameter Polymide particles having a density of 1.05 g/cm³. The seeding particles density was close to that of the working fluid, hence the particles were nearly neutrally buoyant in the measurement region.

For the present set of measurements, a high accuracy multi-pass adaptive cross-correlation technique was used to evaluate the velocity field determined from each pair of particle

images. The signal strength was further optimized by window off-set which minimized particle drop-outs. A sub-pixel accuracy independent of correlation peak shape was achieved and further minimized displacement estimate errors. Measurement uncertainty for the used high accuracy adaptive correlation technique is discussed extensively in Ref. 20.

The final interrogation area, IA, was 16×32 pixels with 75% overlap in both the horizontal and vertical directions. An initial IA of 128×256 pixels was sequentially reduced to the final IA. A dynamic second-order accurate method was used to spatially offset the two IA's during each subsequent iteration cycle by the displacement calculated from previous steps. During each iteration cycle, checks on the correlation's signal-to-noise, as well as, a local comparison of vector attributes with the median value of 3×3 neighbors were used to validate and remove outliers. To remove spurious vectors, a minimum peak height ratio (between 1st and 2nd peak) of 1.2 was used, thereby putting more stringent conditions on peak identification for the subsequent determination of vectors. At each measurement condition, 2000 PIV realizations at a sampling rate of 100 Hz were obtained and used to evaluate the mean and RMS flow field information presented here.

The centerline axial velocities at $0.25D$ downstream of the nozzle, $U_c = 2.06$, 1.66 and 1.36 m/s, for the three Reynolds numbers, were used to normalize reported flow field data.

RESULTS

Figure 2 illustrates radial profiles of the mean axial and radial velocities $0.25D$ away from the lip of the pipe for three Reynolds numbers: $Re_1 = 14{,}602$, $Re_2 = 19{,}135$, and $Re_3 = 24{,}685$. While all velocities are normalized by the centerline axial velocity at the pipe exit, U_c, the axial and radial distances are normalized by the pipe diameter, D. All shown axial velocity distributions obtained in the near-field clearly demonstrate flow symmetry. Furthermore, normalized profiles collapse indicating fully developed pipe conditions.
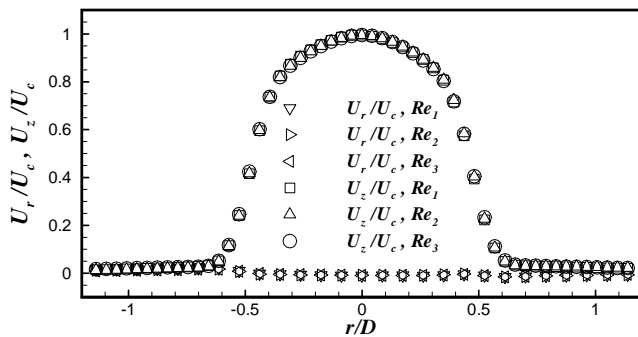

Fig. 2. The radial profiles of axial (U_z/U_c) and radial velocity (U_r/U_c) obtained $0.25D$ downstream the pipe exit for three Reynolds numbers
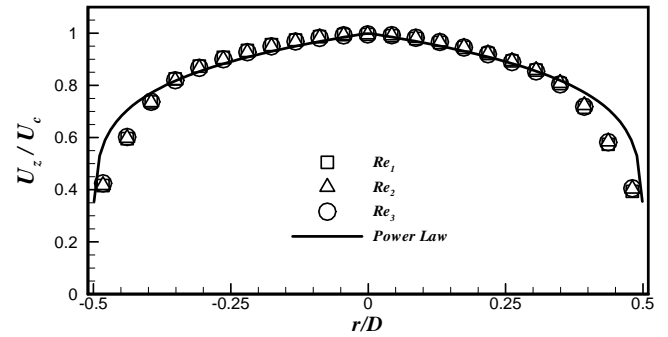

Fig. 3. Comparison between radial profiles of axial velocity at $r/D = 0.25$ and power law

A comparison of U_z/U_c profiles with expected fully developed pipe conditions as approximated by the empirical power-law, $U_z/U_c = 1 - (1 - 2r/D)^{1/n}$, is given in Fig. 3. Good correlation with experimental data is achieved for $1/6^{th}$ power low velocity profile ($n = 6$).

The radial profiles of radial, $u_{r,rms}$, and axial, $u_{z,rms}$, RMS velocities are shown in Fig. 4 (a) and (b), respectively. Close to the pipe, $u_{r,rms}$ values are generally low and do not vary much across the jet. However, $u_{z,rms}$ distribution increases with the Reynolds number and exhibits distinct peaks ($u_{z,rms} \approx 0.1, 0.08, 0.07$) at the edge of the jet due to the development of the turbulent shear layer. Noticeably different RMS value components confirm the anisotropy of the Reynolds normal stresses. Furthermore, variations across the jet core (region defined by $r = \pm0.3D$) are rather small with a local centerline turbulence intensity $u_{z,rms_{CL}} \approx 0.05, 0.04, 0.03$, or $u_{z,rms_{CL}}(U_c/U_b) \approx 0.06, 0.05, 0.04$, which is in good agreement with the expected values. The location $r = \pm0.5D$ can be considered the center of annular shear layer where the velocity fluctuations are appreciably stronger than those found in the jet core.
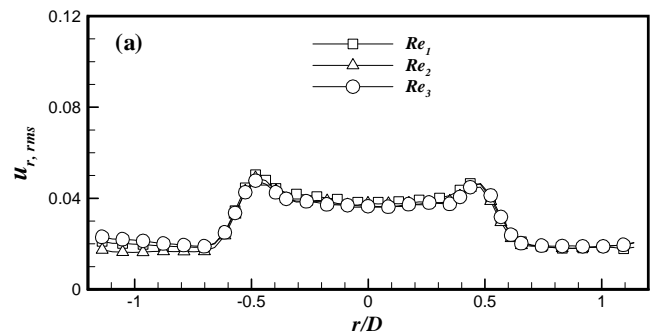

Fig. 4. The radial profiles of RMS velocities, (a) $u_{r,rms}$ and (b) $u_{z,rms}$, $0.25D$ away from the outlet for given Reynolds numbers, Re
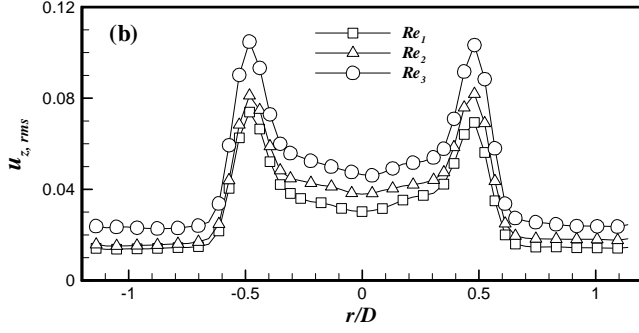
Fig. 4. **The radial profiles of RMS velocities, (a) $u_{r,rms}$ and (b) $u_{z,rms}$, 0.25D away from the outlet for given Reynolds numbers, *Re***

Figure 5 illustrates the normalized mean velocity contours of the jet at $Re_3 \approx 25{,}000$ between $z/D = 0.6$ and 8.3. The jet is axisymmetric with the 'potential core' of approximately uniform flow ($U/U_c \geq 0.9$) below $z/D = 4.4$. Mean flow quantities are now characterized with the help of Figs. 6 and 7.
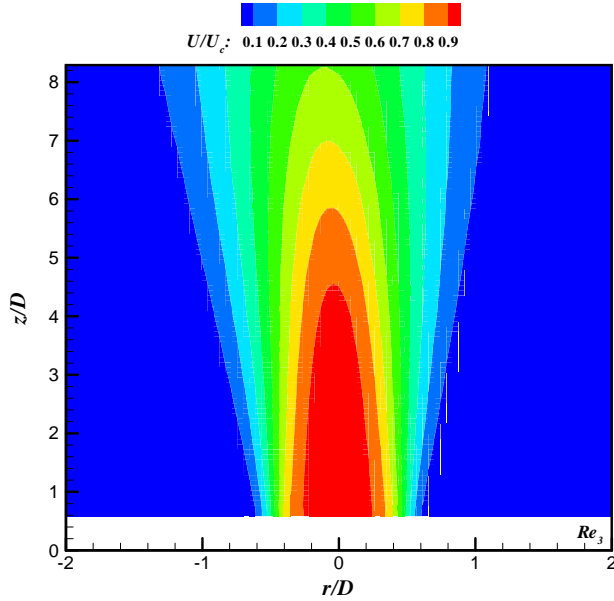

Fig. 5. **Normalized mean velocity contours (U/U_c) between $z/D = 0.6$ and 8.3**

Figure 6 presents the centerline axial and radial mean velocities in the near-field region for three Reynolds numbers. It is apparent that mean velocity is not Reynolds number dependent. The 'potential core' length ($U/U_c \geq 0.9$) of the jet exists up to about 4.4D. Downstream of the potential core region, the centerline velocity decay is typically modeled with a decay equation such as:

$$\frac{U_b}{U_c} = \frac{1}{B}\left(\frac{z}{D} - \frac{z_0}{D}\right) \qquad (1)$$

In this equation, z_0 is the virtual origin, B is the velocity decay coefficient, and D is the pipe diameter. The axial centerline

velocity measurements in the present work collapse onto a straight line and exhibit a decay rate of $B = 5.53$ and a virtual origin $z_0/D = 3.8$. These constants compare well with the existing data, as seen in the Table 1.
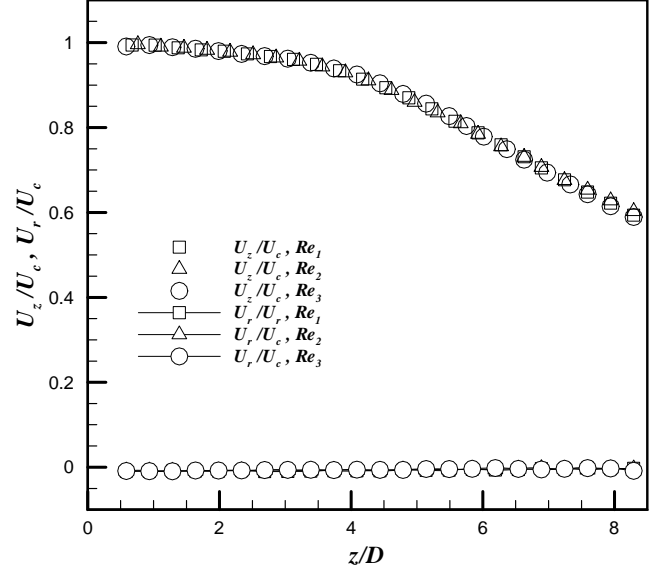

Fig. 6. **Downstream evolution of the mean axial and radial centerline velocities**

Authors	z/D	z_0/D	B
Present study	< 8	3.8	5.53
Wygnanski and Fiedler [21]	< 50	3	5.7
Mi et al. [14]	0-64	3.5	4.48

Table 1   **Centerline mean velocity parameters**

The radial profiles of mean axial velocity at 8 downstream locations are shown in Fig. 7. All velocity distributions demonstrate flow symmetry and independence of *Re* number. The velocity magnitude at the last downstream location, $z/D = 8$, is about 0.61. This is approximately 68% of the 'potential core' value found at $z/D = 4.4$.

Next, the entrainment rate of the ambient fluid into the jet is addressed. The estimate of the local mass flow rate ratio, M/M_e, was obtained from an integral of the mean axial velocity data

$$\frac{M}{M_e} = \frac{\left.\int_0^{D/2} Urdr\right|_z}{\left.\int_0^{D/2} Urdr\right|_{z=0.25D}} \qquad (2)$$

where M_e is the mass flow rate measured at $z/D = 0.25$, and $D/2$ is the radial location at which $U/U_c \approx 1\%$. The result is shown on Fig. 8. The entrainment rate is the highest for $Re_2 \approx 20{,}000$ up to $z/D \approx 7$. The slope of the $Re_1 \approx 15{,}000$ line, initially smaller than that of Re_2, becomes identical downstream of z/D

= 5. However, entrainment rate for the case $Re_3 \approx 25,000$ is substantially lower than that of Re_1 and Re_2 throughout the near-field region. The deviation in entrainment rates observed for Re_3 could be due to the mixing transition phenomenon previously reported by Dimotakis [2] in the $Re = 10,000$-20,000 range.
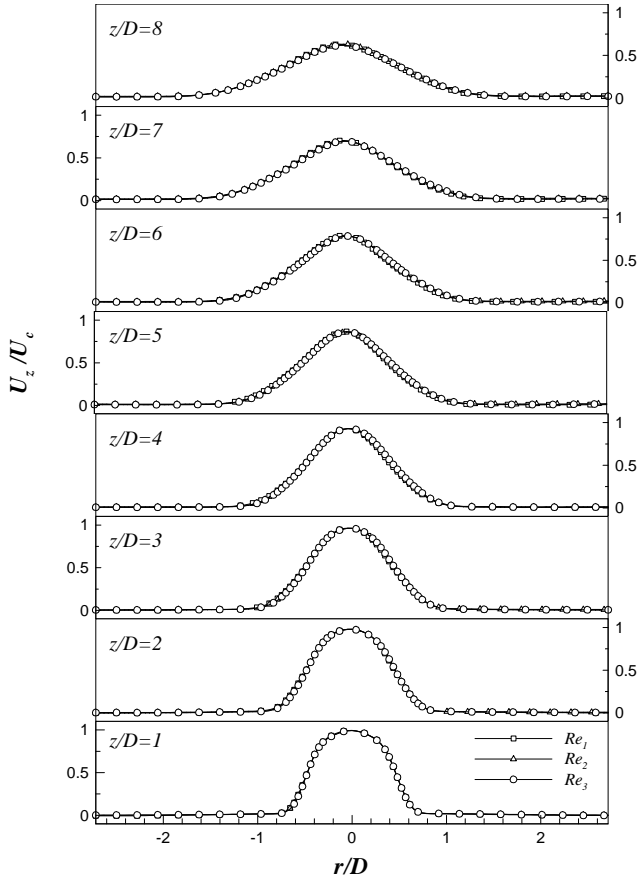

Fig. 7. The radial profiles of mean axial velocity at different axial positions for given Reynolds numbers, *Re*

Figure 9 illustrates jet momentum ratio, J/J_e, based on the mean axial velocity profile measurements

$$\frac{J}{J_e} = \frac{\left.\int_0^{D/2} U^2 r \, dr\right|_z}{\left.\int_0^{D/2} U^2 r \, dr\right|_{z=0.25D}} \qquad (3)$$

where J_e is the jet momentum measured at $z/D = 0.25$. In the absence of buoyancy effects, the jet momentum is conserved up to $z/D = 6$ as $J/J_e = 1$.
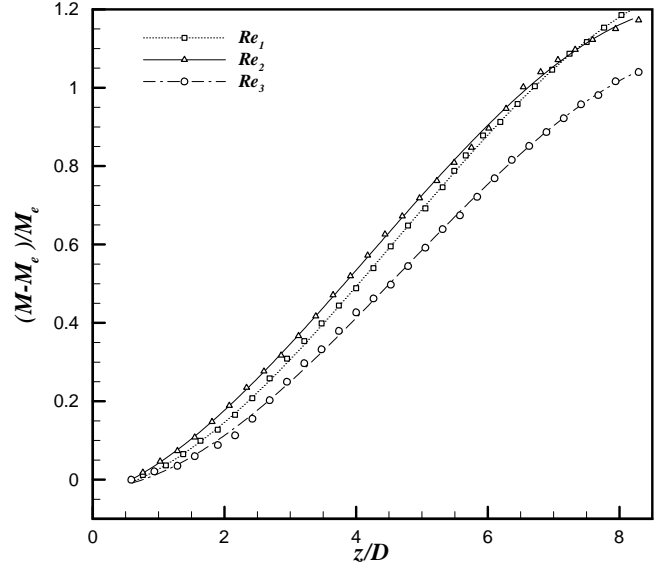

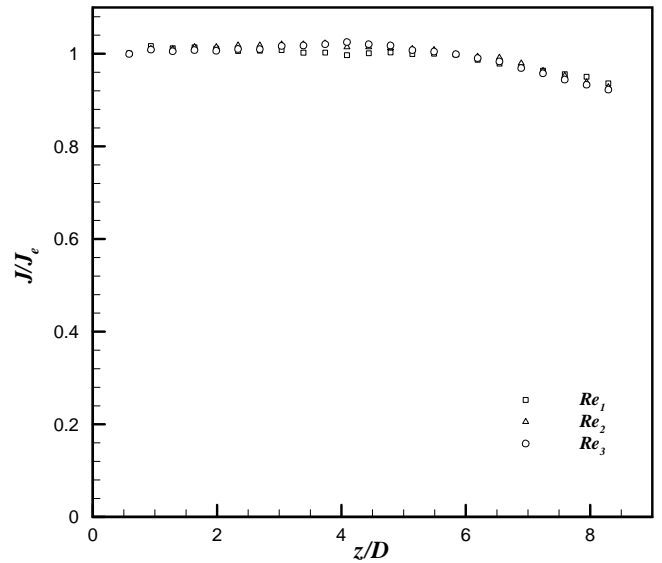**Fig. 8. Entrainment rate of the ambient fluid for given *Re***

Fig. 9. Jet momentum ratio for given *Re*

Contours of the axial RMS velocity obtained for $Re_3 \approx 25,000$ between $z/D = 0.6$ and 8.3 are shown in Fig. 10. Both axial and radial RMS velocity components exhibit distinct peaks at $r/D \approx 0.5$ and $z/D \le 7$. Turbulent flow quantities are now characterized with the help of Figs. 11-13.
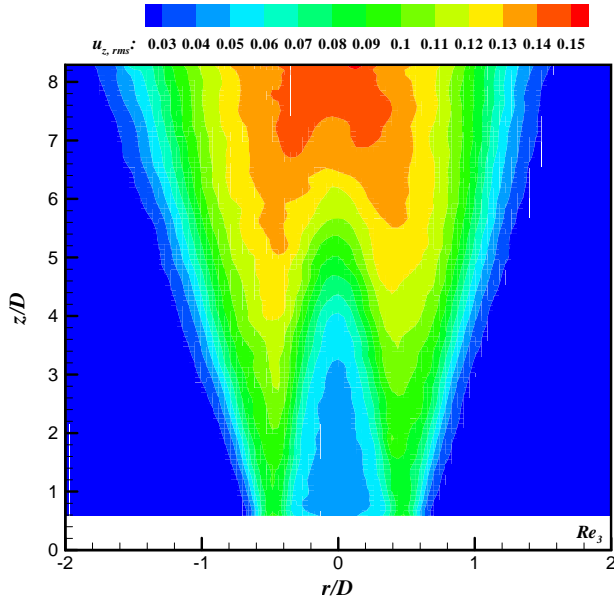
Fig. 10. Contours of the axial RMS velocity, $u_{z,rms}$, between z/D = 0.6 and 8.3

The evolution of the centerline radial ($u_{r,rms}$) and axial ($u_{z,rms}$) RMS velocities is shown in Figs. 11 (a) and (b), respectively. Axial velocity magnitudes increase with the downstream distance and Reynolds number. Only $u_{z,rms}$ values depend substantially on the Reynolds number while $u_{r,rms}$ distributions collapse.
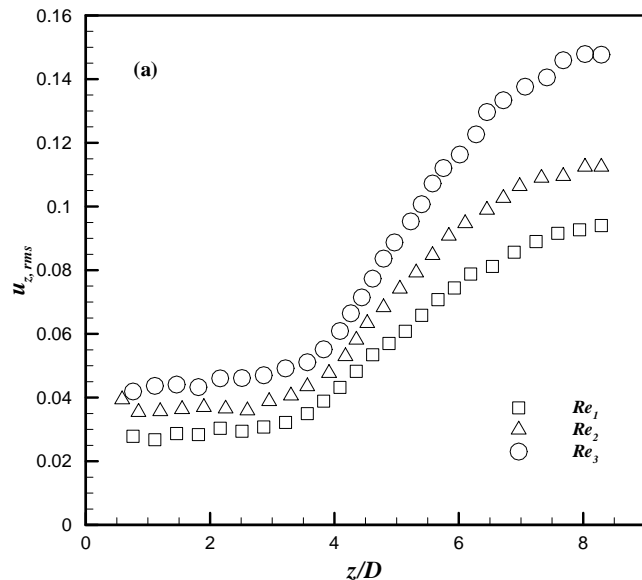

Fig.11. Downstream evolution of the RMS velocities, (a) $u_{z,rms}$, and (b) $u_{r,rms}$ along the centerline for given Reynolds numbers, *Re*
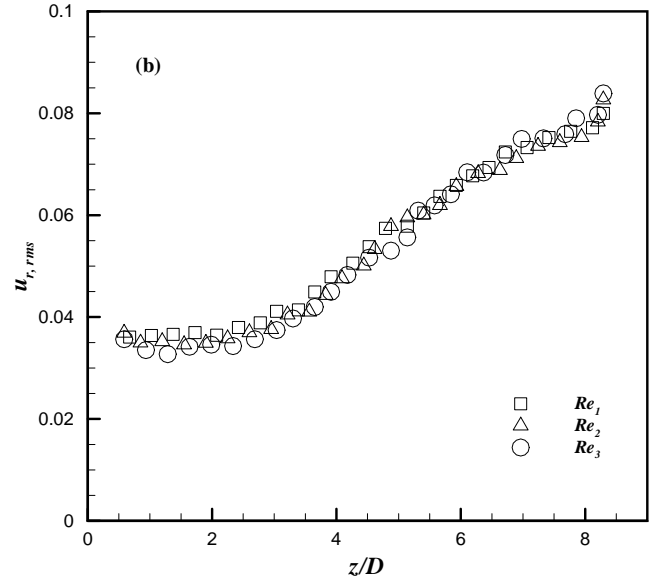

Fig.11. Downstream evolution of the RMS velocities, (a) $u_{z,rms}$, and (b) $u_{r,rms}$ along the centerline for given Reynolds numbers, *Re*

Radial profiles of the axial and radial RMS velocities are shown in Figs. 12 and 13, respectively. Although both velocity distributions exhibit similar trends, only $u_{r,rms}$ profiles collapse. The maximum radial velocity magnitudes are smaller than those of the axial counterparts. The symmetric $u_{r,rms}$ peaks become less distinct for $z/D > 6$ and the relatively flat distribution around the centerline is seen in the last measurement plane. Axial velocity peaks are clearly present at z/D = 6, with remains still visible at the next downstream location. The last measurement plane has just one distinct $u_{z,rms}$ maximum at the centerline.

CONCLUSIONS

A PIV study of the near-field region of a turbulent round water jet issuing from a fully developed pipe flow has been conducted. The two-dimensional flow-field in the plane containing the jet axis was measured in the initial 8*D* region, for three Reynolds numbers: 14,602, 19,135, and 24,685. The selected Reynolds numbers overlap with the previously identified critical Reynolds number range, 10,000-20,000, where flow characteristics of a jet undergo a dramatic transition to a much more chaotic and well-mixed state or fully developed turbulence. Data have been presented for the mean and RMS axial and radial velocity profiles. The downstream variation of the mean axial and radial velocities and $u_{r,rms}$ is independent of the Reynolds number. However, the axial RMS component, $u_{z,rms}$, was found to substantially increase with the Reynolds number. The entrainment rate is the highest for $Re_2 \approx 20,000$, while the observed deviation for $Re_3 \approx 25,000$ could be due to the mixing transition in the critical Reynolds number range.
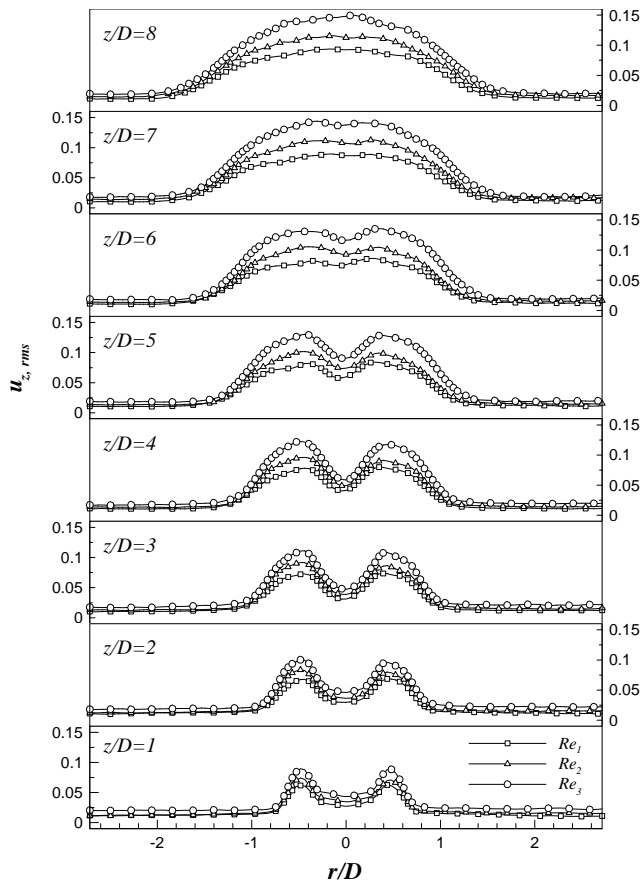
Fig. 12. The radial profiles of RMS velocity, $u_{z,rms}$, at different axial positions for given Reynolds numbers, Re

Fig. 13. The radial profiles of RMS velocity, $u_{r,rms}$, away from the outlet for given Reynolds numbers, Re

REFERENCES

[1] Dimotakis, P. E., Miake-Lye, R. C., and Papantoniou, D. A., 1983, 'Structure and Dynamics of Round Turbulent Jets,' *Phy. Fluids*, **26**, pp. 3185-3192.

[2] Dimotakis, P. E., 2000, 'The Mixing Transition in Turbulent Flows,' *J. Fluid Mech.*, **409**, pp. 69-98.

[3] Ball, C. G., and Pollard, A., 2008, 'A Review of Experimental and Computational Studies of Flow from the Round Jet,' Internal Report: Department of Mechanical and Materials Engineering, Queen's University.

[4] Fellouah, H., Ball, C. G., and Pollard, A., 2009, 'Reynolds Number Effects Within the Development Region of a Turbulent Round Free Jet,' *Int. J. Heat and Mass Transfer*, **52**, pp. 3943-3954.

[5] Shinneeb, A. M., Bugg, J. D., and Balachandar, R., 2008, 'Quantitive investigation of Vortical Structures in the Near-Exit Region of an Axisymmetric Turbulent Jet,' *J. Turbulence*, **9**, 19, pp. 1-20.
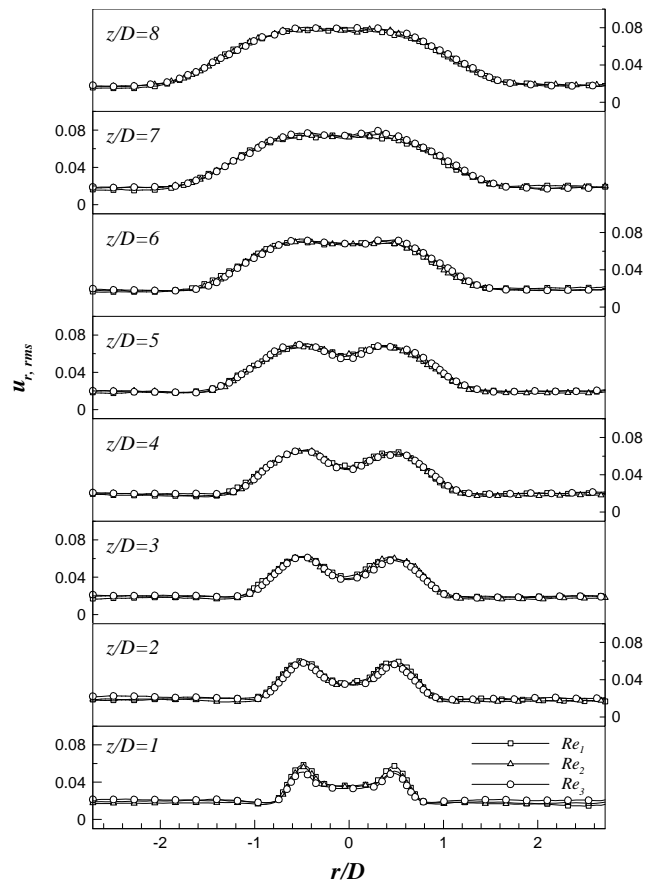
[6] Jung, D., Gamard, S., and George, W. K., 2004, 'Downstream Evolution of the Most Energetic Modes in a Turbulent Axisymmetric Jet at High Reynolds Number. Part 1. The Near-Field Region.' *J. Fluid Mech.*, **514**, pp. 172-204.

[7] Ganapathisubramani, B., Longmire, E. K., and Marusic, I., 2002, 'Investigation of Three Dimensionality in the Near Field of a Round Jet Using Stereo PIV,' *J. Turbulence*, **3**, 16, pp. 1-12.

[8] Ferdman, E., Otugen, M. V., and Kim, S., 2000, 'Effect of Initial Velocity profile on the Development of the Round Jets,' *J. Propulsion and Power*, **16**, 4, pp. 676-686.

[9] Papadopoulos, G., and Pitts, W. M., 1998, 'Scaling the Near-Field Centerline Mixing Behavior of Axisymmetric Turbulent Jets,' *AIAA J.*, **36**, 9, pp. 1635-1642.

[10] Papadopoulos, G., and Pitts, W. M., 1999, 'A Generic Centerline Velocity Decay Curve for Initially Turbulent Axisymmetric Jets,' *J. Fluids Eng.*, **121**, pp. 80-85.

[11] Weisgraber, T. H., and Liepman, D., 1998, 'Turbulent Structure During Transition to Self-Similarity in a Round Jet,' *Exp. Fluids,* **24**, pp. 210-224.

[12] Boguslawski, L., and Popiel, C. O., 1979, 'Flow structure of the Free Round Turbulent Jet in the Initial Region,' *J. Fluid Mech.*, **90**, pp. 531-539.

[13] Xu, G., and Antonia, R. A., 2002, 'Effect of Different Initial Conditions on a Turbulent Round Free Jet,' *Exp. Fluids,* **33**, pp. 677-683.

[14] Mi, J., Nobes, D., and Nathan, G. J., 2001, 'Influence of Jet Exit Conditions on the Passive Scalar Field of an Axisymmetric Free Jet,' *J. Fluid Mech.*, **432**, pp. 91-125.

[15] Mi, J., Nobes, D., and Nathan, G. J., 2001, 'Mixing Characteristics of Axisymmetric Free Jets Issuing from a Contoured Nozzle, an Orifice Plate and a Pipe,' *J. Fluids Eng.*, **123**, pp. 878-883.

[16] Richards, C. D., and Pitts, W. M., 1993, 'Global Density Effects on the Self-Preservation Behavior of Turbulent Free jets,' *J. Fluid Mech.*, **245**, pp. 417-435.

[17] Bogey, C., and Bailly, C., 2006, 'Large Eddy Simulations of Transitional Round Jets: Influence of the Reynolds Number on Flow Development and Energy Dissipation,' *Phy. Fluids*, **18**, pp. 1-14.

[18] Mcllwain, S., and Pollard, A., 2002, 'Large Eddy Simulation of the Effects of Mild Swirl on the Near Field of a Round Free Jet,' *Phy. Fluids*, **14**, 2, pp. 653-661.

[19] Olsson, M., Fuchs, L., 1996, 'Large Eddy Simulation of the Proximal Region of a Spatially Developing Circular Jet,' *Phy. Fluids*, **8**, 8, pp. 2125-2137.

[20] Westergaard, Madsen, Marassi, and Tomasini, 2003, 'Accuracy of PIV Signals in Theory and Practice,' 5th International Symposium on Particle Image Velocimetry, Busan, Korea, September 22-24, Paper 3301.

[21] Wygnanski, I., Fiedler, H., 1969, 'Some Measurements in the Self-Preserving Jet,' *J. Fluid Mech.*, **38**, pp. 577-612.